Materials Advances

Accepted Manuscript

This article can be cited before page numbers have been issued, to do this please use: A. Govardhan, L. A. Guerrero-León, V. V. Shilovskikh, F. Paulus, B. Rivkin and Y. Vaynzof, *Mater. Adv.*, 2026, DOI: 10.1039/D6MA00389C.

ROYAL SOCIETY OF CHEMISTRY

rsc.li/materials-advances

View Article Online
DOI: 10.1039/D6MA00389C

ARTICLE

From Spin Coating to Zone Casting: Process Dependence and Challenges in Scaling Quasi-2D Perovskite Films

Received 00th January 20xx,
Accepted 00th January 20xx

DOI: 10.1039/x0xx00000x

Akshay Govardhan,†[a,b] L. Andrés Guerrero-León,†[a,b] Vladimir Shilovskih,[a,b] Fabian Paulus,[a] Boris Rivkin,[a,b] and Yana Vaynzof *[a,b]

Two-dimensional (2D) hybrid organic-inorganic perovskites are promising materials for photovoltaics due to their tunable optoelectronic properties and enhanced stability compared to three-dimensional (3D) perovskites. However, efficiency limitations stem from the distribution and orientation of their multi-quantum well structures, necessitating improvements in thin film fabrication methods, especially when transitioning from lab-scale to large-scale deposition. This study compares quasi-2D perovskite ($BA_2MA_4Pb_5I_{16}$) thin films prepared by spin-coating and zone-casting – a scalable method for large-area deposition - examining the effects of solution temperature, substrate temperature, and host solvent ratios on their structural and morphological properties. Both methods demonstrated increased crystallite size with increasing temperature, with zone-casting leading to significantly larger grains of up to 8 µm. On the other hand, spin-coating provides superior control over film orientation, leading to high photovoltaic performance of 18.1%, highlighting the need to develop new strategies for control of texture across large areas of quasi-2D perovskite layers

Introduction

The growing global demand for clean and sustainable energy has accelerated the development of advanced photovoltaic (PV) technologies. In this context, hybrid organic-inorganic halide perovskites have emerged as one of the most promising candidates for next-generation solar cells. Since the pioneering work of Tsutomu Miyasaka[1] in 2009, in which methylammonium lead iodide ($MAPbI_3$) was first employed in solar cells, perovskite-based photovoltaics have evolved rapidly, achieving power conversion efficiencies (PCE) exceeding 26% [2–4] and challenging established technologies such as crystalline silicon and thin-film cadmium telluride.

Hybrid metal-halide perovskites exhibit a unique combination of properties that make them highly attractive for PV applications. Their direct bandgap, large absorption coefficients, and long charge carrier diffusion lengths enable efficient light harvesting, while their tuneable optoelectronic properties allow precise engineering for optimal device performance [5–8]. Additionally, low-cost, low-temperature, and large-scale solution processing methods offer a pathway toward scalable manufacturing [9–11]. Despite these advantages, long-term operational stability remains a central challenge. Sensitivity to oxygen, moisture, illumination, and thermal stress [12–15] leads to chemical and structural degradation, thereby hindering performance and limiting device lifetime.

A promising approach to enhance environmental and operational stability of metal halide perovskites is to reduce their dimensionality. In particular, quasi-two-dimensional (2D) halide perovskites have attracted significant attention as alternatives to three-dimensional (3D) perovskites due to their superior environmental, chemical, and photostability, along with their tunable optoelectronic properties [16–18]. These materials generally follow the formula $A'_2A_{n-1}B_nX_{3n+1}$, where A′ is a bulky organic cation, and *n* denotes the number of inorganic layers separated by these spacer cations. Although a target *n* value is typically defined during solution preparation, quasi-2D perovskite films typically exhibit a distribution of phases spanning multiple low-*n* values, often including 3D-like phases.

As a result, solar cells based on quasi-2D perovskites typically exhibit lower efficiencies than those based on 3D perovskites. This limitation is largely due to the random orientation and uneven distribution of low-dimensional phases within the film, which hinder efficient charge transport and extraction [18–20]. In these low-*n* phases, metal-halide octahedra form quantum wells, while the organic spacer cations act as potential barriers, creating a multi-quantum-well structure that confines charge carriers. For efficient operation in vertically stacked solar cells, low-*n* phases must be oriented perpendicular to the substrate plane to facilitate charge transport. Moreover, a favourable energetic landscape between phases is essential to enable exciton dissociation and carrier transport.

Consequently, recent research has focused on developing strategies to control the dimensional structure of quasi-2D perovskite films, including hot-casting and solvent engineering approaches that can effectively control the orientation and phase distribution [21–24]. While these methods have proven

[a] Leibniz Institute for Solid State and Materials Research Dresden, Helmholtzstr. 20, 01069 Dresden, Germany
[b] Chair for Emerging Electronic Technologies, Technical University of Dresden, Nöthnitzer Str. 61, 01187 Dresden, Germany

View Article Online
DOI: 10.1039/D6MA00789C

effective for fabricating efficient small-area devices via spin-coating, their applicability to large-area, scalable deposition techniques remains largely unexplored.

In this study, we present a systematic investigation of quasi-2D perovskite thin films prepared using both conventional spin coating and the scalable meniscus-guided deposition technique of zone casting. This method was first introduced in 1983 by Burda et al. for the crystallization of organic molecules in a polymer matrix [25], and has since then been utilized for a variety of materials [26–30], including 3D perovskites [31]. We analyse the influence of deposition method, processing temperature, and solvent mixture composition on the structural, optical, and morphological characteristics of Ruddlesden–Popper (RP) $BA_2MA_4Pb_5I_{16}$ (BA = butylammonium, $\langle n \rangle$ = 5) thin films. By examining these texture-control strategies — such as solvent engineering and hot-casting —we identify key limitations of these methods and highlight the need to develop new strategies tailored to the scalable processing of quasi-2D perovskites.

Experimental

Materials

Anhydrous dimethylformamide (DMF, 99.9%) and dimethylsulfoxide (DMSO, 99.8%) were purchased from Sigma-Aldrich. 2-(3,6-dimethoxy-9*H*-carbazol-9-yl)ethyl]phosphonic acid (MeO-2PACz), bathocuproine (BCP), lead iodide (PbI_2) were purchased from TCI, while n-butylammonium iodide (BAI), and methylammonium iodide (MAI) were purchased from GreatCellSolar. (6,6)-Phenyl C61 butyric acid methyl ester (PCBM) was purchased from Luminescence Technology Corp. Unpatterned ITO substrates (25 mm x 25 mm, thickness: 1.1 mm) and patterned ITO (12 mm x 12 mm) were purchased from Ossila and PsiOTech Ltd., respectively.

Substrate Preparation

Substrates were sequentially cleaned in deionized water, acetone, and isopropanol using 5-minute sonication steps, followed by drying under a nitrogen stream. Oxygen plasma treatment was applied for 10 minutes to improve surface wettability.

Spin-coating Film Deposition

Spin-coating was performed under controlled dry-box conditions (<1.7% RH). ITO substrates (12 mm x 12mm) and precursor solutions were preheated from 60 °C to 100 °C and maintained prior to deposition. The films were spin-coated at 5000 rpm for 30 seconds and annealed at 100 °C for 5 minutes.

Zone-casting Film Deposition

This method utilized glass slides measuring 25 mm x 25 mm as substrates. We employed a custom-built zone-casting instrument, depicted in **Figure S1**. The figure labels key components of the apparatus, such as a substrate holder, syringe holder, and nozzle, which can be heated to a specific temperature. The gap between the casting bar and the substrate was maintained at 1 mm, the angle was set to 0°, and the casting speed and injection rate were systematically examined to finalize fabrication parameters. Most of these parameters—except for the gap and angle between the cylindrical bar and the substrate—are controlled through a custom software interface, CasToroid, developed using a Raspberry Pi.

The casting was conducted under ambient conditions (35–55% RH). Under a systematic variation of casting speed (0.05–15 mm/s) and injection rate (0.3–2 µL/s), the optimal parameter set for our reference samples were: 5mm/s (casting speed) and 0.3 µL/s (injection rate). The ITO substrates and precursor solutions were heated up from 60 to 100°C prior deposition, and later annealed at 120 °C for 20 minutes.

Physical Characterization

X-ray diffraction (XRD) was carried out on a Bruker D8 Discover diffractometer with Cu Kα radiation (1.5418 Å). UV-Vis absorption spectra were recorded using a Jasco V-770 spectrophotometer. Scanning electron microscopy (SEM) was performed using a Gemini SEM 500 ZEISS electron microscope with InLens, HE-SE2, and BSE detectors. Grain sizes were analysed using ImageJ software from several processed SEM micrographs. For each processing condition, the grains were manually measured to obtain statistically representative average grain sizes. Film thicknesses were measured by Veeco Dektak 150 profilometer. The PL spectra were recorded by an Ocean Optics QE65 spectrometer connected to an integrating sphere and the samples were excited with a laser at a fixed excitation wavelength of 405 nm with a nominal power of 100 mW.

Device Fabrication

Patterned ITO and fully covered ITO glass substrates (1.2 × 1.2 cm) were cleaned sequentially in an ultrasonic bath with deionized water, acetone, and isopropyl alcohol (IPA) for 5 min each. Substrates were dried with a stream of nitrogen gas and treated with oxygen plasma for 10 min to enhance surface wettability. The hole transport layer (HTL) solution of MeO-2PAC (1 mM) in methanol was spin-coated at 3000 rpm for 30 s. Substrates were then annealed at 100 °C for 10 min. The perovskite precursor solution was prepared by dissolving BAI, MAI, and PbI_2 in a solution mixture of DMF:DMSO (19:1 and 9:1) at a concentration of 0.8 M. The solution was stirred at 80 °C overnight until a homogeneous mixture was obtained. Subsequently, 40 µL of precursor solution at a specific temperature was deposited onto the HTL while the sample was kept at the same temperature as the solution (ranging from 60 °C to 100 °C). The spin-coating process was carried out at a rotation speed of 5000 rpm for 30 s. After spin-coating, the films were subjected to an annealing treatment at 100 °C for 5 min in a hotplate. The samples were transferred to an N_2-filled glovebox, and 35 µL of a solution of PCBM in chlorobenzene was spin-coated onto the perovskite layer at 2000 rpm for 30 s followed by annealing at 100 °C for 5 min. 30 µL of BCP in isopropanol were finally spin-coated at 4000 rpm for 30 s.

View Article Online
DOI: 10.1039/D6MA00389C

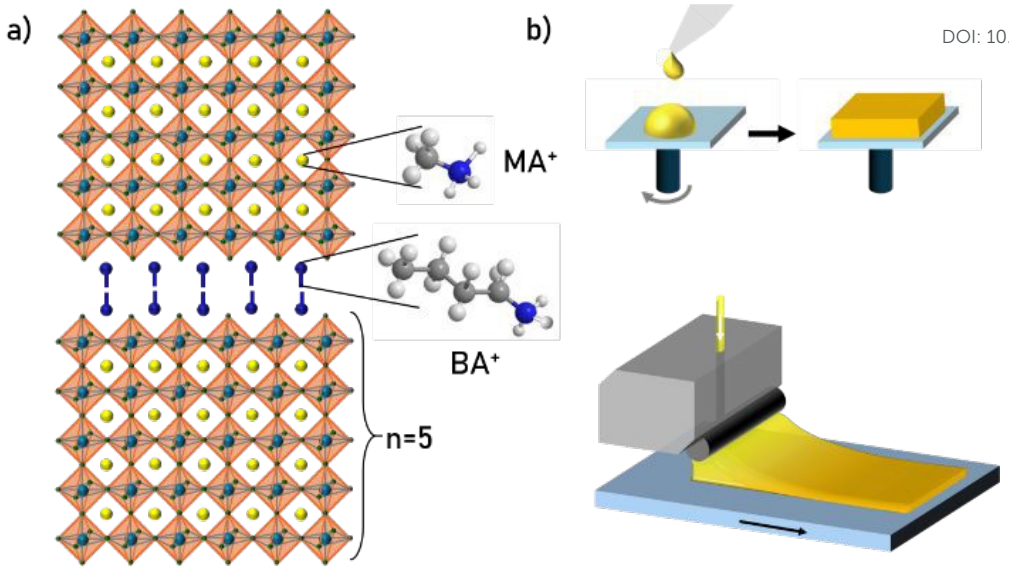

Figure 1. Schematic illustration of a) the BA2MA4Pb5I16 (<n>=5) perovskite composition and b) the two deposition techniques (spin-coating and zone-casting) used in this work.

80 nm of Ag was deposited on top via thermal evaporation to complete the device structure. A shadow mask was used to define the solar cell's active area (4.5 mm^2).

Results and Discussion

Many reports have identified solvent engineering and temperature control as crucial parameters for achieving controlled orientation in 2D perovskite phases, given their inherently anisotropic behaviour [18,23]. In multilayer devices such as solar cells, improving the out-of-plane alignment is crucial to enhance charge transport from the photoactive layer to the neighbouring transport layers[7]. While these strategies have been widely applied for spin-coated films, their effectiveness in large-area deposition methods remains unexplored.

Here, we employ zone-casting, a meniscus-guided deposition technique. In this process, the perovskite solution is continuously dispensed through a heated nozzle and spread with a bar over the entire width of the substrate (Figure S1). The substrate is moved at a defined speed while maintaining a fixed nozzle height, allowing the meniscus to form and move across the surface. As the solvent evaporates, the solute crystallizes as a thin film. This process is different to thin film deposition by spin-coating, where film formation is driven by centrifugal forces and rapid solvent ejection, leading to near-instantaneous, spatially homogeneous nucleation (Figure 1). The zone-casting process involves several independent parameters, including casting speed, solution injection rate (solution supply rate), nozzle height, casting angle, and processing temperature. In this study, the parameters were reduced to casting speed, injection rate, solution and substrate temperature. A precursor solution dissolved in a DMF:DMSO mixture (9:1 volume ratio, 0.8M) was used for the identification of suitable zone casting paramters. Detailed experimental parameters are provided in the Experimental Section.

To identify suitable zone-casting processing conditions, films were deposited over a wide range of casting speeds (0.05-15 mm s^{-1}) and injection rates (0.3-2 µL s^{-1}), followed by characterization using polarized optical microscopy (Figure S2). The results reveal that the film microstructure is highly sensitive to variations in deposition parameters, which govern local supersaturation at the meniscus and dictate nucleation density and growth dynamics. However, the interplay between the surface-solution interaction and solvent-evaporation flux introduces significant complexity, making it difficult to distinguish between different growth regime[28]. Despite this, films fabricated at different processing temperatures using 0.3 µL s^{-1} and a casting speed of 5 mm s^{-1} consistently exhibited uniform morphology with no pinholes, voids, or needle-like crystallites (Figure S3). This parameter set provides an optimal balance between deposition speed, film uniformity, and material utilization, and was therefore selected for the following experiments.

The crystallization of perovskite films is strongly governed by solvent removal dynamics. In quasi-2D systems, antisolvent treatment is typically not required, making solvent evaporation under hot-casting conditions the dominant factor controlling crystallization kinetics. Given the distinct boiling points of DMF (153 °C) and DMSO (189 °C), tuning the solvent ratio in combination with the substrate temperature enables precise control over evaporation rates and intermediate phase formation[32]. To explore the impact of these effects, films were deposited at solution-substrate temperatures ranging from 60 °C to 100 °C using DMF:DMSO ratios of 9:1 and 19:1. For direct comparison, identical processing conditions were applied to both spin-coated (SC) and zone-cast (ZC) films.

X-ray diffraction (XRD) patterns (Figure 2a-d) confirm the formation of perovskite in all films. Two dominant diffraction peaks are observed at 14.1° and 28.4°, corresponding to the

View Article Online
DOI: 10.1039/D6MA00389C

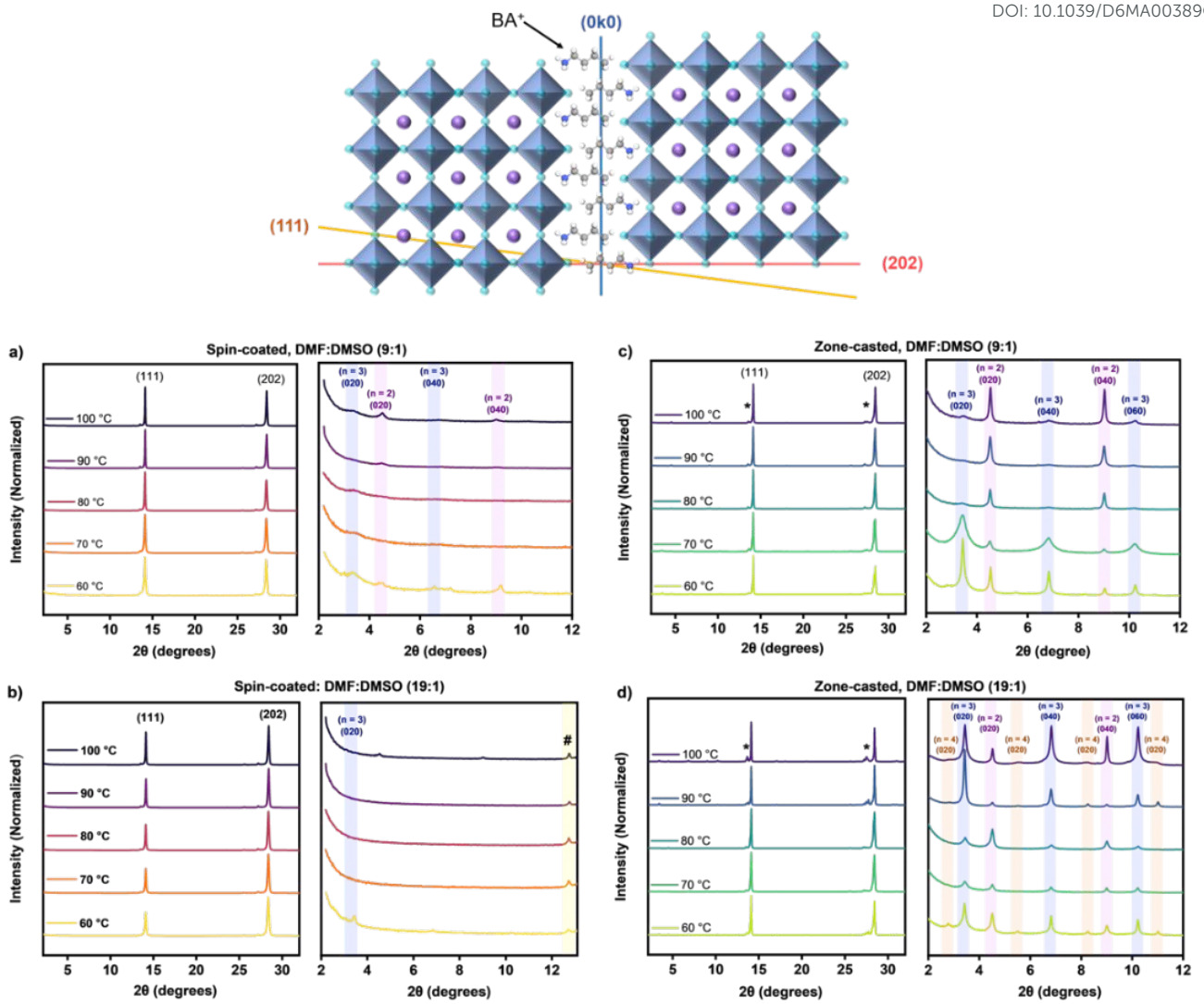

Figure 2. (Up) Schematic of the RP quasi-2D perovskite structure, with the relevant (*hkl*) reflections indicated for better interpretation of the preferred crystal orientations. X-ray diffractograms of spin-coated (a, b) and zone-cast (c, d) thin films. The films were deposited using precursor solutions with 9:1 (a, c) and 19:1 (b, d) DMF:DMSO volume ratios.

(111) and (202) planes of the 3D-like perovskite phase [23,24]. In addition, weaker peaks at 13.7° and 27.7° are also observed in zone-cast films, which can be attributed to the tetragonal phase of $MAPbI_3$. This phase exhibits lower symmetry than the cubic phase and suggests a degree of structural disorder or incomplete phase transition[33].

The structure shown in Figure 2 eases the visualization of the orientation of these crystal planes. Specifically, the (111) plane indicates the presence of tilted crystals, while the (202) plane is orthogonal to the quasi-2D planes, showing that the diffraction intensities of the (202) and (0k0) planes are inversely correlated [23,34]. Therefore, the crystallographic relationship of the (111) and (202) reflections ratio was used to estimate the degree of texture and relative out-of-plane orientation in quasi-2D perovskite films (also expressed as $I_{28.4°}/I_{14.1°}$).

In quasi-2D perovskite films, the interpretation of peak intensities in θ-2θ XRD patterns is complex due to the coexistence of low-*n* and 3D-like phases, and the strong anisotropic nature of layered perovskites. Therefore, variations in peak intensities may come not only from changes in preferential orientation, but also from differences in phase distribution and local structural disorder. Nevertheless, we provide a simple analysis based on the $I_{28.4°}/I_{14.1°}$ relationship to estimate the texture and relative orientation of vertically and horizontally oriented phases in the absence of more advanced techniques.

The $I_{28.4°}/I_{14.1°}$ ratios (Figure 3) show a clear trend for spin-coated films: increasing the DMF fraction (19:1) results in a higher degree of texture than with the 9:1 ratio. This behaviour is attributed to the reduced dipole moment of the solvent mixture and the diminished formation of DMSO–PbI_2 intermediate complexes [35,36] [37] As a result, this triggers a more direct and faster transition from the precursors to the perovskite phase, favouring better vertical growth. The temperature-dependent $I_{28.4°}/I_{14.1°}$ ratios at higher DMF

View Article Online
DOI: 10.1039/D6MA00380C

fractions (19:1) further reveal that higher processing temperatures reduce the relative intensity of the (202) peak, indicating a loss of relative vertical orientation due to accelerated nucleation and rapid crystal growth, which limit the formation of oriented crystals. When using a higher DMSO fraction (9:1), the solution-substrate temperature appears to have little effect on the 3D-like phases. We propose that the increased DMSO content stabilizes the precursor-solvent interactions, making the resulting film microstructure less sensitive to thermal variations by slowing the overall crystallization.

On the other hand, zone cast films consistently exhibit stronger (111) reflections than (202) reflections under all conditions, indicating a higher degree of crystal lattice anisotropy. This suggests that zone-casting deposition process exerts a dominant kinetic influence on the crystal growth that override the subtler crystallization effects observed in spin-coating.

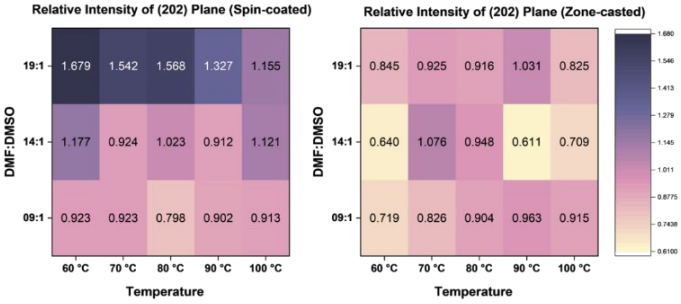

Figure 3. Intensity ratio ($I_{28.4°}/I_{14.1°}$) relationship between the (111) and (202) planes of the spin-coated and zone-casted $BA_2MA_4Pb_5I_{16}$ films.

At low diffraction angles (2θ < 12°), spin-coated films show only weak signatures of low-*n* phases (*n* = 2, 3) for both solvent mixtures (Figure 2a-b). The presence of strong (202) reflections with a negligible intensity of quasi-2D (0*k*0) reflections suggests a preferentially aligned orientation perpendicular to the substrate, which is beneficial for vertical charge transport. In contrast, zone cast films (Figure 2c-d) exhibit stronger low-angle reflections, indicating the presence of more horizontally oriented planes of low-*n* perovskite phases [38].

Furthermore, the dominant low-*n* phase varies with processing temperatures. For example, in the 9:1 solvent system, lower temperatures favor n = 3 phases, while higher temperatures promote n = 2 phases. This trend reverses for the 19:1 solvent mixture. These observations highlight the strong coupling between solvent composition and evaporation kinetics for phase formation. However, it is worth noting that the overall contribution of low-*n* reflections remains relatively small compared to that of 3D-like phases, even in zone cast films, where they are comparatively more intense than in spin-coated samples. This offers a favourable perspective for photovoltaic applications, as it implies that at least partial out-of-plane alignment is preserved, which could facilitate charge transport.

The crystallite quality was evaluated by extracting the full width at half maximum (FWHM) of the main diffraction peaks (Figure 4). A decrease in FWHM with increasing temperature is consistently observed for spin-coated films, indicating improved crystallinity and larger coherent domain sizes at higher temperatures. ZC films, on the other hand, exhibit a less systematic trend. This behaviour is also observed by the crystallite-size evolution shown in Figure S4.

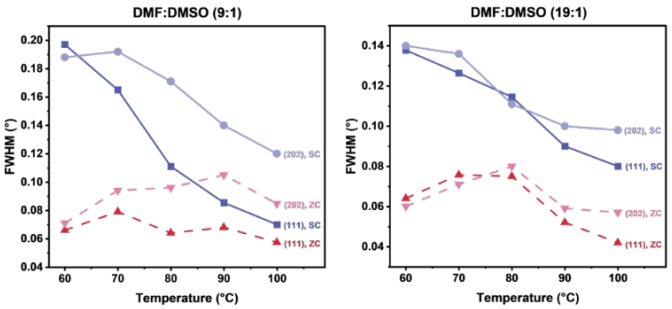

Figure 4. Full width at half maximum (FWHM) of the X-ray diffraction peaks of spin-coated (solid lines) and zone-cast (dashed lines) $BA_2MA_4Pb_5I_{16}$ films processed from 9:1 and 19:1 DMF:DMSO precursor mixtures.

Zone cast films are significantly thicker than spin-coated films (Figure 5), reflecting the fundamental differences in deposition mechanisms. While spin-coating relies on centrifugal thinning, zone-casting involves continuous material supply, promoting thicker film formation. For spin-coated films, thickness increases with solution-substrate temperature due to accelerated solvent evaporation and faster crystallization. However, at higher temperatures, the thickness becomes less sensitive to solvent composition, indicating a transition governed by processing temperature

The films deposited by zone-casting exhibit significantly greater thicknesses overall due to the continuous solution supply and meniscus-mediated deposition mechanism. The thickness evolution depends strongly on the solvent composition. Films prepared using a 9:1 ratio show a gradual increase in thickness with increasing processing temperature, following a trend similar to that observed for spin-coated films. In contrast, films deposited from the 19:1 solvent mixture exhibit a non-monotonic behavior, with the thickness initially increasing and subsequently decreasing at higher temperatures.

This behaviour can be interpreted using the framework proposed by Chang et al.[39], in which three wet-thickness regions (I, II, III) are defined according to the balance between surface tension, viscous, and inertial forces within the coating bead. In this model, the film thickness (t) is related to the capillary number (Ca) following Figure 5, inset. Ca is defined as $\mu V/\sigma$, where μ is the solvent viscosity.[40] Since the solvent viscosity decreases with increasing temperature ($\mu \propto e^{1/T}$), the capillary number is also affected by the processing temperature. Consequently, temperature alters the mixture at the meniscus,

leading to the thickness variations observed in the 19:1 film, consistent with a transition from Region $III \rightarrow I$. At elevated temperatures, rapid solvent evaporation additionally promotes meniscus recession and destabilization, further reducing the deposited film thickness.[26,28,41]. The distinct behaviour observed for the 9:1 solvent system can be attributed to the higher DMSO content, which increases the overall viscosity of the precursor solution (μ_{DMF}= 0.8 cP, μ_{DMSO}= 1.99 cP at 25° C) and shifts the transition between regions to different temperatures.

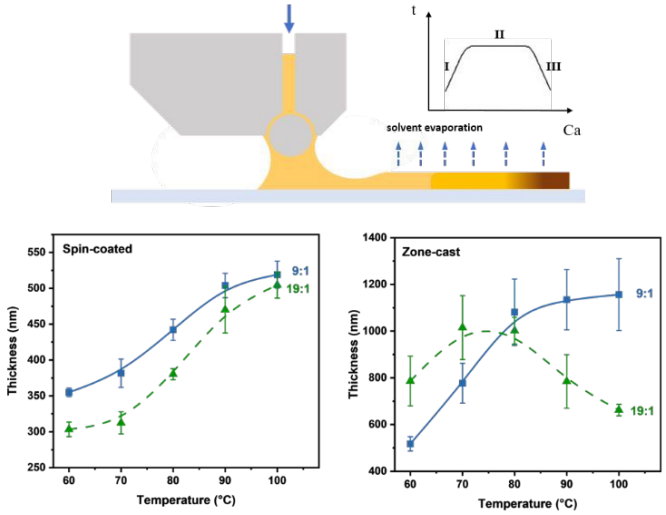

Figure 5. Thickness of $BA_2MA_4Pb_5I_{16}$ films deposited from 9:1 (straight lines) and 19:1 (dashed lines) DMF:DMSO precursor mixtures at different processing temperatures (60 - 100° C), using spin-coating (left) and zone-casting (right).

UV–Vis absorption spectra confirm the coexistence of low-*n* and 3D-like phases in all films (Figure S5).[16] Photoluminescence (PL) spectra (Figure 6) exhibit a dominant emission peak at ~780 nm, corresponding to the 3D-like phase. A red shift is observed in the zone cast films as compared to spin-coated films. One possible explanation for this is that their emission is dominated by lower-bandgap 3D domains that are formed due to enhanced phase segregation, where low-*n* and 3D-like domains are spatially separated rather than forming an intermixed structure. On the other hand, spin-coated films are deposited in a layered gradient, leading to emission at higher energies.

Additionally, zone-cast films exhibit stronger quasi-2D emission (450–650 nm), indicating reduced energy transfer to 3D phases. This suggests inefficient exciton funnelling due to spatial separation, which disrupts the energy-transfer pathway, leading to radiative recombination of the low-n excitons and higher quasi-2D PL. In contrast, the intermixed structure in SC films ensures a shorter domain spacing, leading to efficient energy transfer and a quenching of the quasi-2D emission, with enhanced 3D emission.[42,43]

The microstructure of the films was examined by scanning electron microscopy (SEM) (Figure 7). SC films prepared with 9:1 solvent ratio at lower temperatures exhibit significant defects, such as numerous pinholes and voids. These defects arise from the relatively higher boiling point of the mixture, which leads to a non-uniform solvent evaporation and inhomogeneous

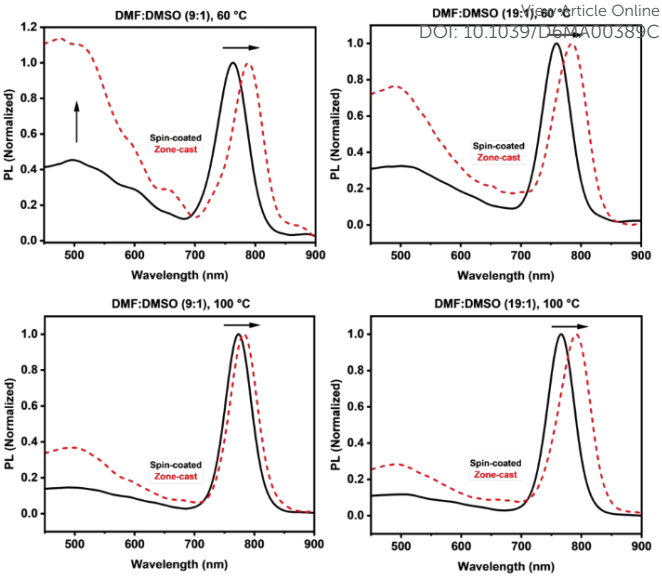

Figure 6. Normalized PL spectra of the zone-casted (red line) and spin-coated (black line) films using different DMF:DMSO solvent mixtures and deposited at 60°C (left) and 100°C (right).

crystallization. Increasing the processing temperature improves film uniformity by enhancing molecular mobility, allowing grains to merge and grow. As a result, the number of grain boundaries decreases, thereby reducing the defect density.[44] The 19:1 formulation leads to fewer defects even at lower spin-coating temperatures, attributed to a lower evaporation rate resulting from a lower extent of DMSO-complex formation. However, at 100 °C, crack formation is observed propagating along grain boundaries, likely due to rapid solvent evaporation and associated mechanical stress. Zone-cast films exhibit similarly homogeneous surfaces with significantly larger grain sizes. This highlights that zone-casting can also fabricate homogeneous films, with grain sizes far larger than those of the spin-coated layers (Figure S6). Despite their improved uniformity, macroscopic fractures are evident in nearly all zone-cast layers. The formation of these cracks is primarily due to the larger thickness and the entrapment of solvents during crystallization.

A cross-sectional SEM analysis further reveals differences in film formation. The spin-coated films exhibit a comparatively compact and intermixed phase distribution throughout the film thickness (Figure S7a-b), which suggests a more uniform crystallization process. In contrast, the zone-cast films display structural heterogeneity and visible phase segregation (Figure S7, c-d). Distinct regions with different orientations and morphologies can be observed, indicating the coexistence of domains of different crystal organizations. Such phase segregation contributes to the altered optical response observed in the PL measurements and is expected to disrupt carrier-extraction pathways between the quasi-2D domains and the 3D-like phase.

View Article Online
DOI: 10.1039/D6MA00389C

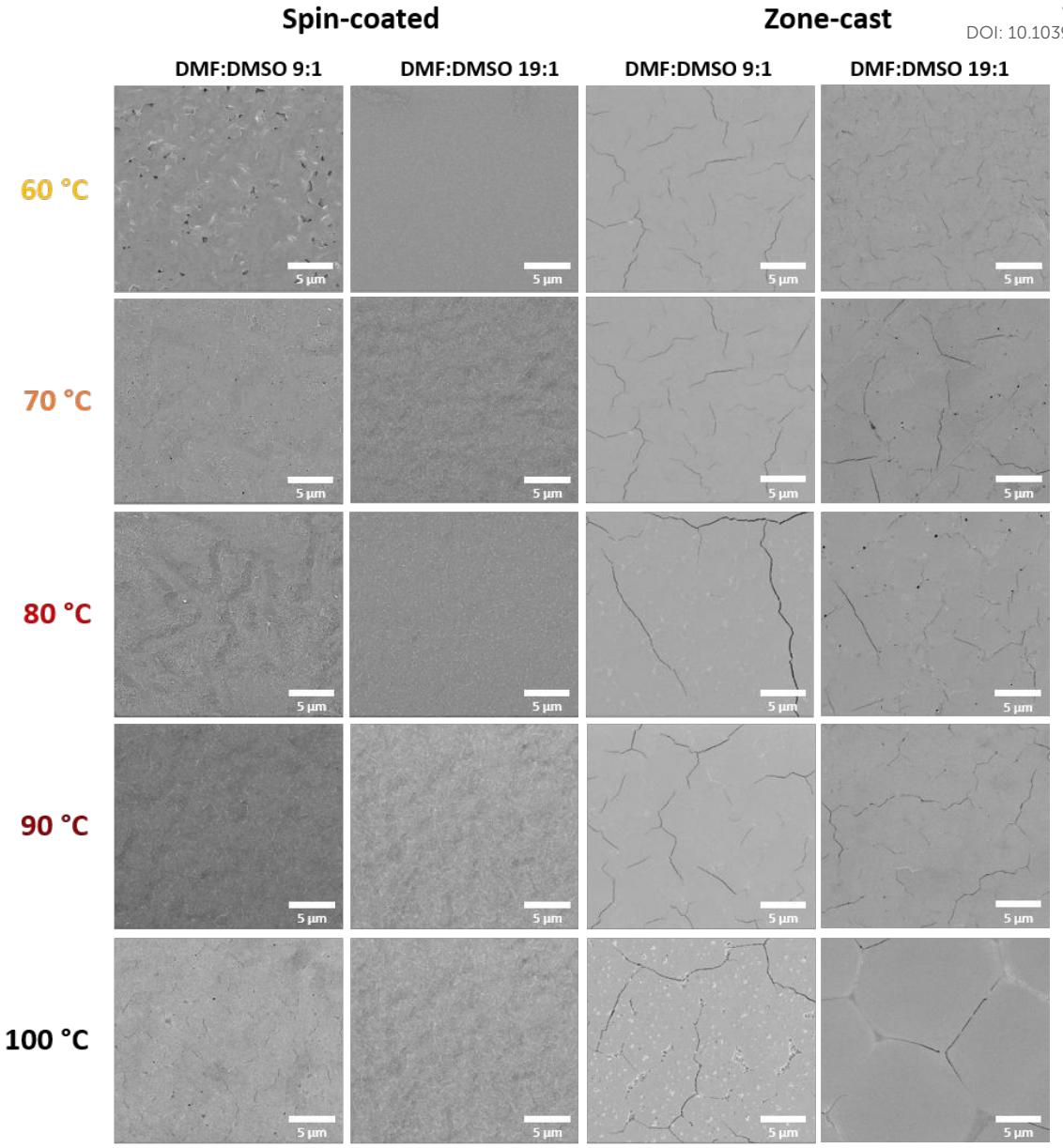

Figure 7. SEM images of thin films prepared by spin-coating and zone-casting from precursor solutions with 9:1 and 19:1 DMF:DMSO volume ratios, processed at solution–substrate temperatures ranging from 60 °C to 100 °C.

Grain size analysis (Figure 8) shows a consistent increase with temperature for both deposition methods, attributed to a reduced nucleation density and accelerated grain-boundary migration at higher temperatures, consistent with Ostwald ripening theory. At all temperatures, zone-cast films exhibit significantly larger grains than spin-coated films due to the fundamentally different deposition pathways. Spin-coating induces homogeneous nucleation across the substrate, leading to a high nucleation density. In contrast, zone-casting deposits the film through directional evaporation with a moving meniscus, where supersaturation develops locally and gradually. The prolonged adduct lifetime allows the grains to grow to much larger dimensions during crystallization.

When varying the solvent fraction, spin-coated films with increasing DMSO content lead to larger grains due to the slower solvent evaporation and the stabilization of intermediate solvent-precursor complexes. The mixture provides more time for solute diffusion and crystal growth, which leads to larger grains. Interestingly, the influence of ratios differs significantly between the two deposition methods, where lower DMSO content results in larger grains. This behaviour is likely related to the decrease in nucleation density within the deposited layer, allowing the grains to expand more freely before convergence.

These results underscore that the crystallization mechanisms in spin-coating and zone-casting are fundamentally different, reaffirming how even similar parameters distinctly influence grain size, phases distribution, and overall film microstructure for each technique.

View Article Online
DOI: 10.1039/D6MA00380D

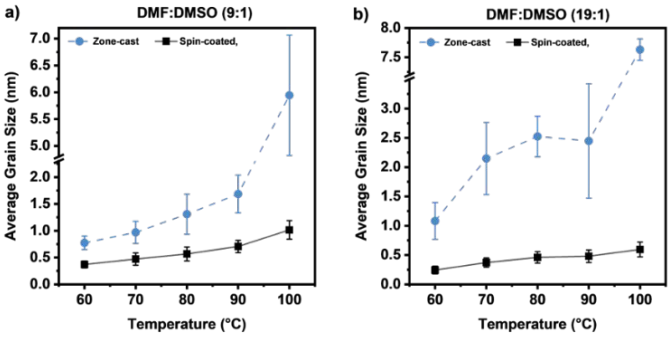

Figure 8. Average grain size measured from the SEM images of 9:1 (left) and 19:1 (right) DMF:DMSO using spin-coating and zone-casting. The error bar indicates the standard deviation of the distribution of grain sizes.

Overall, the differences in film properties can be attributed to the distinct crystallization mechanisms related to each fabrication technique. In spin-coating, the crystallization kinetics of quasi-2D films are predominantly governed by the solvent evaporation rate during the rapid spinning process [45]. In contrast, zone-casting involves an interplay of additional factors, including the solution-supplying flux, meniscus dynamics, and the local concentration gradient.[28] This shows that conventional strategies, such as solvent engineering and hot-casting, are often effective for texture control in spin-coated films but are less effective when applied to zone-cast films. While our results provide clear evidence of these differences, further work is necessary to fully understand the detailed kinetics of crystallization during zone-casting and how the formation of quasi-2D and 3D domains.

Our results observed in the zone-cast films are expected to significantly affect their integration in solar devices. The presence of low-*n* phases and strong phase segregation can hinder efficient out-of-plane charge transport due to their anisotropic conductivity. In addition, the large thickness and macroscopic cracks are also expected to negatively impact device integration, inducing shunting pathways.

Therefore, due to fabrication constraints, photovoltaic characterization was limited to spin-coated films, as zone-casting was proved unsuccessful for integration. Nevertheless, we suggest that they would be unlikely to deliver meaningful photovoltaic performance even if device integration were feasible.

Spin-coated layers were incorporated as active materials in solar cells with an inverted architecture (glass/ITO/MeO2PACz/perovskite/PCBM/BCP/Ag). Figure 9 shows the photovoltaic performance of the films deposited from 9:1 and 19:1 DMF:DMSO precursor solutions at different processing temperatures. Devices based on the 9:1 ratio consistently exhibited lower performance than those fabricated with the 19:1 ratio. The optimal temperature for the 9:1 device was 70 °C, while the optimal performance for the 19:1 device was 60 °C, reaching a maximum power conversion efficiency of 18.1%. The shelf-life stability of one of the latter devices (encapsulated) was tracked under normal air conditions for over 350h, maintaining ~95% of its original performance (Figure S8).

Outlook and Conclusions

This study systematically compared the structural and morphological properties of quasi-2D perovskite ($BA_2MA_4Pb_5I_{16}$) thin films fabricated via spin-coating and zone-casting by varying solution-substrate temperatures and DMF:DMSO solvent ratios. While spin-coating enables uniform solvent removal and rapid film formation under controlled laboratory conditions, zone-casting introduces additional complexities associated with meniscus-guided deposition, including directional solvent evaporation, local supersaturation gradients and continuous solution supply. These factors fundamentally alter the crystallization dynamics of quasi-2D perovskites and make the control of phase distribution, orientation, and morphology considerably more challenging during scalable processing.

Spin-coated films demonstrated superior vertical orientation and crystallinity, leading to photovoltaic performance of up to 18.1%. In contrast, zone-cast films

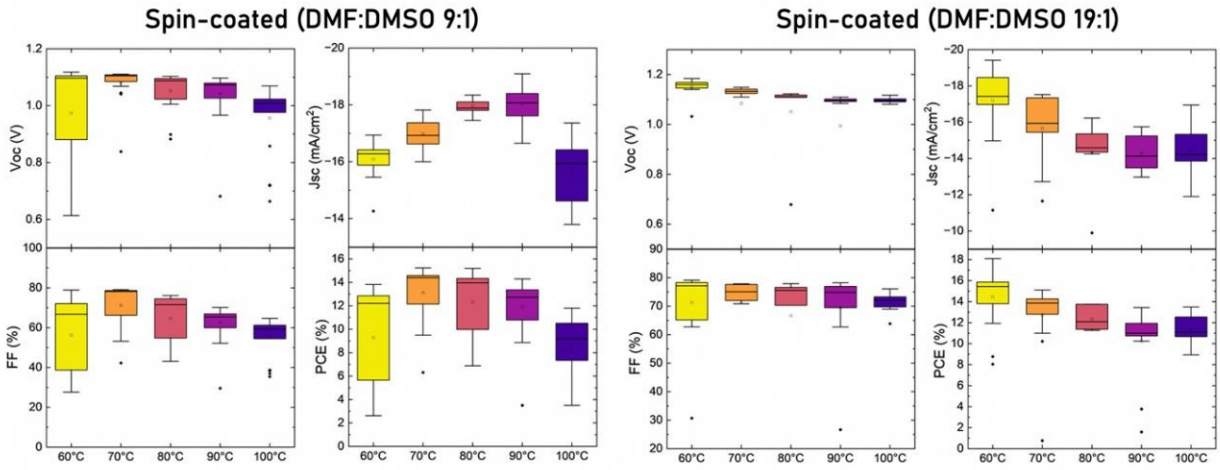

Figure 9. Photovoltaic performance parameters of solar cells based on spin-coated quasi-2D perovskite films deposited from 9:1 and 19:1 DMF:DMSO precursor solutions at varying processing temperatures (60-100 °C).

View Article Online
DOI: 10.1039/D6MA00389C

consistently exhibited more horizontally oriented low-*n* phases, and less control over the morphology. Microstructural cracks were observed in zone-cast films, most likely due to mechanical stress induced by solvent removal. Despite these challenges, zone-casting promoted the growth of significantly larger, well-defined crystalline grains—characteristics considered advantageous for charge transport and reduced recombination—highlighting the potential of zone-casting for scalable quasi-2D perovskite fabrication.

While spin-coating remains more suitable for lab-scale device fabrication, zone-casting holds promise for scalable production, provided its fabrication parameters and environmental factors are carefully optimized. Our study demonstrates that strategies applied to spin-coating such as solvent engineering and hot-casting are not directly applicable to the optimization of zone-cast quasi-2D films. Therefore, we emphasize in the necessity of exploring and elucidating the complex kinetics of phase formation observed in large-area printing technologies. Moreover, future efforts should focus on substrate surface treatments and further tuning of solution properties to enhance film uniformity and trigger vertical orientation.

Author contributions

† A.G, and L.A.G.L. contributed equally to this work.

Conflicts of interest

There are no conflicts to declare.

Acknowledgements

L.A.G.L. and Y.V. acknowledge the M-ERA.NET grant "PHANTASTIC" call 2021 [R.8003.22], supported by the SMWK.

References

1 A. Kojima, K. Teshima, Y. Shirai and T. Miyasaka, *J. Am. Chem. Soc.*, 2009, **131**, 6050–6051.
2 A. D. Taylor, Q. Sun, K. P. Goetz, Q. An, T. Schramm, Y. Hofstetter, M. Litterst, F. Paulus and Y. Vaynzof, *Nat. Commun. 2021 121*, 2021, **12**, 1–11.
3 J. Liu, Y. He, L. Ding, H. Zhang, Q. Li, L. Jia, J. Yu, T. W. Lau, M. Li, Y. Qin, X. Gu, F. Zhang, Q. Li, Y. Yang, S. Zhao, X. Wu, J. Liu, T. Liu, Y. Gao, Y. Wang, X. Dong, H. Chen, P. Li, T. Zhou, M. Yang, X. Ru, F. Peng, S. Yin, M. Qu, D. Zhao, Z. Zhao, M. Li, P. Guo, H. Yan, C. Xiao, P. Xiao, J. Yin, X. Zhang, Z. Li, B. He and X. Xu, *Nature*, 2024, **635**, 596–603.
4 A. S. R. Bati, Y. L. Zhong, P. L. Burn, M. K. Nazeeruddin, P. E. Shaw and M. Batmunkh, *Commun. Mater. 2023 41*, 2023, **4**, 1–24.
5 A. K. Jena, A. Kulkarni and T. Miyasaka, *Chem. Rev.*, 2019, **119**, 3036–3103.
6 T. Wu, Z. Qin, Y. Wang, Y. Wu, W. Chen, S. Zhang, M. Cai, S. Dai, J. Zhang, J. Liu, Z. Zhou, X. Liu, H. Segawa, H. Tan, Q. Tang, J. Fang, Y. Li, L. Ding, Z. Ning, Y. Qi, Y. Zhang and L. Han, *Nano-Micro Lett.*, 2021, **13**, 1–18.
7 Z. Hu, Z. Lin, J. Su, J. Zhang, J. Chang and Y. Hao, *Sol. RRL*, 2019, **3**, 1900304.
8 D. W. DeQuilettes, S. M. Vorpahl, S. D. Stranks, H. Nagaoka, G. E. Eperon, M. E. Ziffer, H. J. Snaith and D. S. Ginger, *Science (80-.).*, 2015, **348**, 683–686.
9 F. Wang, Y. Han, D. Duan, C. Ge, H. Hu and G. Li, *Energy Rev.*, 2022, **1**, 100010.
10 Z. Li, T. R. Klein, D. H. Kim, M. Yang, J. J. Berry, M. F. A. M. Van Hest and K. Zhu, *Nat. Rev. Mater. 2018 34*, 2018, **3**, 1–20.
11 X. Tian, S. D. Stranks, J. Huang, V. M. Fthenakis, Y. Yang and F. You, *Energy Environ. Sci.*, 2025, **18**, 194–213.
12 S. Khatoon, S. Kumar Yadav, V. Chakravorty, J. Singh, R. Bahadur Singh, M. S. Hasnain and S. M. M. Hasnain, *Mater. Sci. Energy Technol.*, 2023, **6**, 437–459.
13 N. Ahn and M. Choi, *Adv. Sci.*, 2024, **11**, 2306110.
14 C. Ma, F. T. Eickemeyer, S. H. Lee, D. H. Kang, S. J. Kwon, M. Grätzel and N. G. Park, *Science (80-.).*, 2023, **379**, 173–178.
15 R. Guo, D. Han, W. Chen, L. Dai, K. Ji, Q. Xiong, S. Li, L. K. Reb, M. A. Scheel, S. Pratap, N. Li, S. Yin, T. Xiao, S. Liang, A. L. Oechsle, C. L. Weindl, M. Schwartzkopf, H. Ebert, P. Gao, K. Wang, M. Yuan, N. C. Greenham, S. D. Stranks, S. V. Roth, R. H. Friend and P. Müller-Buschbaum, *Nat. Energy 2021 610*, 2021, **6**, 977–986.
16 L. N. Quan, M. Yuan, R. Comin, O. Voznyy, E. M. Beauregard, S. Hoogland, A. Buin, A. R. Kirmani, K. Zhao, A. Amassian, D. H. Kim and E. H. Sargent, *J. Am. Chem. Soc.*, 2016, **138**, 2649–2655.
17 C. Liang, H. Gu, Y. Xia, Z. Wang, X. Liu, J. Xia, S. Zuo, Y. Hu, X. Gao, W. Hui, L. Chao, T. Niu, M. Fang, H. Lu, H. Dong, H. Yu, S. Chen, X. Ran, L. Song, B. Li, J. Zhang, Y. Peng, G. Shao, J. Wang, Y. Chen, G. Xing and W. Huang, *Nat. Energy 2020 61*, 2020, **6**, 38–45.
18 T. Lv, Y. Liang, F. Li, X. Yang, J. Huang and R. Zheng, *Sci. China Physics, Mech. Astron.*, 2023, **66**, 1–17.
19 G. Grancini and M. K. Nazeeruddin, *Nat. Rev. Mater. 2018 41*, 2018, **4**, 4–22.
20 X. Li, J. M. Hoffman and M. G. Kanatzidis, *Chem. Rev.*, 2021, **121**, 2230–2291.
21 X. Li, K. Li, B. Wang, X. Zhang, S. Yue, Y. Li, Q. Chen, S. Li, T. Yue, H. Zhou, Y. Zhang, X. Li, X. Zhang, T. Yue, Y. Zhang, K. Li, B. Wang, S. Yue, Y. Li, Q. Chen, S. Li and H. Zhou, *Adv. Funct. Mater.*, 2021, **31**, 2107675.
22 H. Tsai, W. Nie, J. C. Blancon, C. C. Stoumpos, R. Asadpour, B. Harutyunyan, A. J. Neukirch, R. Verduzco, J. J. Crochet, S. Tretiak, L. Pedesseau, J. Even, M. A. Alam, G. Gupta, J. Lou, P. M. Ajayan, M. J. Bedzyk, M. G. Kanatzidis and A. D. Mohite, *Nat. 2016 5367616*, 2016, **536**, 312–316.
23 W. L. Tan and C. R. McNeill, *Appl. Phys. Rev.*, DOI:10.1063/5.0076665/2835369.
24 R. Jiang, T. Tian, B. Ke, Z. Kou, P. Müller-Buschbaum, F. Huang, Y. B. Cheng and T. Bu, *Next Mater.*, 2023, **1**, 100044.
25 L. Burda, A. Tracz, T. Pakula, J. Ulanski and M. Kryszewski, *J.*

View Article Online
DOI: 10.1039/D6MA00389C

Phys. D. Appl. Phys., 1983, **16**, 1737.
26 A. Tracz, T. Pakula and J. K. Jeszka, *Mater. Sci. Pol.*
27 C. Ren, L. Cao and T. Wu, *Small*, 2023, **19**, 2300151.
28 O. Yildiz, Z. Wang, M. Brzezinski, S. Wang, Z. Li, J. J. Michels, P. W. M. Blom, W. Pisula and T. Marszalek, *Adv. Funct. Mater.*, 2024, **34**, 2314131.
29 M. Chen, B. Peng, S. Huang, P. Kwok Leung Chan, M. Chen, B. Peng, S. Huang and P. K. L Chan, *Adv. Funct. Mater.*, 2020, **30**, 1905963.
30 F. Paulus, J. U. Engelhart, P. E. Hopkinson, C. Schimpf, A. Leineweber, H. Sirringhaus, Y. Vaynzof and U. H. F. Bunz, *J. Mater. Chem. C*, 2016, **4**, 1194–1200.
31 P. Fassl, S. Ternes, V. Lami, Y. Zakharko, D. Heimfarth, P. E. Hopkinson, F. Paulus, A. D. Taylor, J. Zaumseil and Y. Vaynzof, *ACS Appl. Mater. Interfaces*, 2019, **11**, 2490–2499.
32 J. Han, R. H. Kim, S. Huang, J. Kim and J. S. Yun, *Sol. RRL*, 2024, **8**, 2400262.
33 P. S. Whitfield, N. Herron, W. E. Guise, K. Page, Y. Q. Cheng, I. Milas and M. K. Crawford, *Sci. Reports 2016 61*, 2016, **6**, 1–16.
34 J. A. Steele, E. Solano, D. Hardy, D. Dayton, D. Ladd, K. White, P. Chen, J. Hou, H. Huang, R. A. Saha, L. Wang, F. Gao, J. Hofkens, M. B. J. Roeffaers, D. Chernyshov and M. F. Toney, *Adv. Energy Mater.*, DOI:10.1002/AENM.202300760.
35 L. A. Guerrero-León, J. R. Bautista-Quijano, H. Heffner, V. Shilovskikh, R. Campos, B. Rivkin and Y. Vaynzof, *Adv. Energy Mater.*, 2024, **14**, 2402916.
36 R. Vidal, J. A. Alberola-Borràs, S. N. Habisreutinger, J. L. Gimeno-Molina, D. T. Moore, T. H. Schloemer, I. Mora-Seró, J. J. Berry and J. M. Luther, *Nat. Sustain. 2020 43*, 2020, **4**, 277–285.
37 J. R. Bautista-Quijano, O. Telschow, F. Paulus and Y. Vaynzof, *Chem. Commun.*, 2023, **59**, 10588–10603.
38 L. Mao, C. C. Stoumpos and M. G. Kanatzidis, *J. Am. Chem. Soc.*, 2019, **141**, 1171–1190.
39 Y. R. Chang, H. M. Chang, C. F. Lin, T. J. Liu and P. Y. Wu, *J. Colloid Interface Sci.*, 2007, **308**, 222–230.
40 X. Ding, J. Liu and T. A. L. Harris, *AIChE J.*, 2016, **62**, 2508–2524.
41 X. Gu, L. Shaw, K. Gu, M. F. Toney and Z. Bao, *Nat. Commun. 2018 91*, 2018, **9**, 1–16.
42 L. Lei, D. Seyitliyev, S. Stuard, J. Mendes, Q. Dong, X. Fu, Y.-A. Chen, S. He, X. Yi, L. Zhu, C.-H. Chang, H. Ade, K. Gundogdu, F. So, L. Lei, J. Mendes, Q. Dong, X. Fu, S. He, X. Yi, L. Zhu, F. So, D. Seyitliyev, S. Stuard, H. Ade, K. Gundogdu, Y. Chen and C. Chang, *Adv. Mater.*, 2020, **32**, 1906571.
43 N. Yantara, A. Bruno, A. Iqbal, N. Fadilah Jamaludin, C. Soci, S. Mhaisalkar, N. Mathews, N. Yantara, A. Bruno, A. Iqbal, C. Soci, N. F. Jamaludin, S. Mhaisalkar and N. Mathews, *Adv. Mater.*, 2018, **30**, 1800818.
44 J. L. Barnett, V. L. Cherrette, C. J. Hutcherson and M. C. So, *Adv. Mater. Sci. Eng.*, 2016, **2016**, 4126163.
45 R. Das and A. Chanda, *Nano-Size Polym. Prep. Prop. Appl.*, 2016, 283–306.

From Spin Coating to Zone Casting: Process Dependence and Challenges in Scaling Quasi-2D Perovskite Films

View Article Online
DOI: 10.1039/D6MA00389C

Akshay Govardhan, L. Andrés Guerrero-León, Vladimir Shilovskih, Fabian Paulus, Boris Rivkin and Yana Vaynzof*

Leibniz-Institute for Solid State and Materials Research Dresden, Helmholtzstraße 20, 01069 Dresden, Germany

Chair for Emerging Electronic Technologies, Technical University of Dresden, Nöthnitzer Str.61, 01187 Dresden, Germany

The datasets generated during and/or analysed during the current study are not publicly available due to potential protection, but are available from the authors on reasonable request.